AGU PUBLICATIONS

JGR

Journal of Geophysical Research: Solid Earth

RESEARCH ARTICLE
10.1002/2016JB013570

Key Points:
- The new seismicity near Fox Creek is clustered in time and space
- Clusters are induced by hydraulic fracturing of the Duvernay Formation
- Strike-slip motion with two clusters confirmed on north-south fault orientations

Supporting Information:
- Supporting Information S1

Correspondence to:
R. Schultz,
Ryan.Schultz@aer.ca

Citation:
Schultz, R., R. Wang, Y. J. Gu, K. Haug, and G. Atkinson (2017), A seismological overview of the induced earthquakes in the Duvernay play near Fox Creek, Alberta, *J. Geophys. Res. Solid Earth*, *122*, 492–505, doi:10.1002/2016JB013570.

Received 19 SEP 2016
Accepted 7 DEC 2016
Accepted article online 9 DEC 2016
Published online 18 JAN 2017
Corrected 11 FEB 2017

This article was corrected on 11 FEB 2017. See the end of the full text for details.

A seismological overview of the induced earthquakes in the Duvernay play near Fox Creek, Alberta

Ryan Schultz[1], Ruijia Wang[2], Yu Jeffrey Gu[2], Kristine Haug[1], and Gail Atkinson[3]

[1]Alberta Geological Survey, Edmonton, Alberta, Canada, [2]Department of Physics, University of Alberta, Edmonton, Alberta, Canada, [3]Department of Earth Sciences, University of Western Ontario, London, Ontario, Canada

Abstract This paper summarizes the current state of understanding regarding the induced seismicity in connection with hydraulic fracturing operations targeting the Duvernay Formation in central Alberta, near the town of Fox Creek. We demonstrate that earthquakes in this region cluster into distinct sequences in time, space, and focal mechanism using (i) cross-correlation detection methods to delineate transient temporal relationships, (ii) double-difference relocations to confirm spatial clustering, and (iii) moment tensor solutions to assess fault motion consistency. The spatiotemporal clustering of the earthquake sequences is strongly related to the nearby hydraulic fracturing operations. In addition, we identify a preference for strike-slip motions on subvertical faults with an approximate 45° *P* axis orientation, consistent with expectation from the ambient stress field. The hypocentral geometries for two of the largest-magnitude (M ~4) sequences that are robustly constrained by local array data provide compelling evidence for planar features starting at Duvernay Formation depths and extending into the shallow Precambrian basement. We interpret these lineaments as subvertical faults orientated approximately north-south, consistent with the regional moment tensor solutions. Finally, we conclude that the sequences were triggered by pore pressure increases in response to hydraulic fracturing stimulations along previously existing faults.

1. Introduction

Anthropogenic activities have the potential to cause or trigger earthquakes [e.g., *Raleigh et al*., 1976], as suggested by numerous case studies of mining, dam impoundment, fluid production, disposal/injection, geothermal systems, and hydraulic fracturing [*Davies et al*., 2013]. Globally, numerous cases of earthquakes related to hydraulic fracturing operations have been discussed [*Holland*, 2013; *Clarke et al*., 2014; *Friberg et al*., 2014; *Skoumal et al*., 2015a]. Similarly, seismicity within the Western Canada Sedimentary Basin (WCSB) has been linked to petroleum resource development operations including production [*Horner et al*., 1994; *Baranova et al*., 1999], disposal [*Schultz et al*., 2014], and hydraulic fracturing [BC Oil and Gas Commission, 2012; *Schultz et al*., 2015a, 2015b; *Babaie Mahani et al*., 2016] (Figure 1a). Among these cases, the recent increase in seismicity in the WCSB (e.g., Figure 1b) has been associated with hydraulic fracturing operations [*Atkinson et al*., 2016], most notably within the Duvernay Formation near the town of Fox Creek, Alberta. Earthquakes within this region began on 1 December 2013 [*Schultz et al*., 2015a] and have continued to date (data set for this paper ends February 2016). In response to the increasing public concern over induced seismic hazard [*Atkinson et al*., 2015] and the first moderate-sized earthquake in the Fox Creek area (M 3.6 23 January 2015 SS6), the Alberta Energy Regulator introduced a traffic light protocol as a part of the new monitoring and reporting requirements [*Alberta Energy Regulator*, 2015]. These requirements stipulate that Duvernay operators in the Fox Creek area must report all adjacent yellow light events ($M_L \geq 2.0$) and implement mitigation strategies at this level. A red light event ($M_L \geq 4.0$) requires the immediate cessation of operations.

This study focuses on the seismogenic well completions in the Duvernay Formation near Fox Creek, a region that has experienced some of the largest-magnitude earthquakes related to hydraulic fracturing. We begin by familiarizing the reader with the Duvernay Formation and development operations therein. Then we describe a marked increase in the rate of seismicity in the regions that roughly coincides with the beginning of development operations. The earthquakes clearly cluster in time, space, and focal mechanism, and the cluster occurrences can be uniquely related to a well or well pad completion to a high degree of confidence. Much of the data used in these analyses were provided by the public

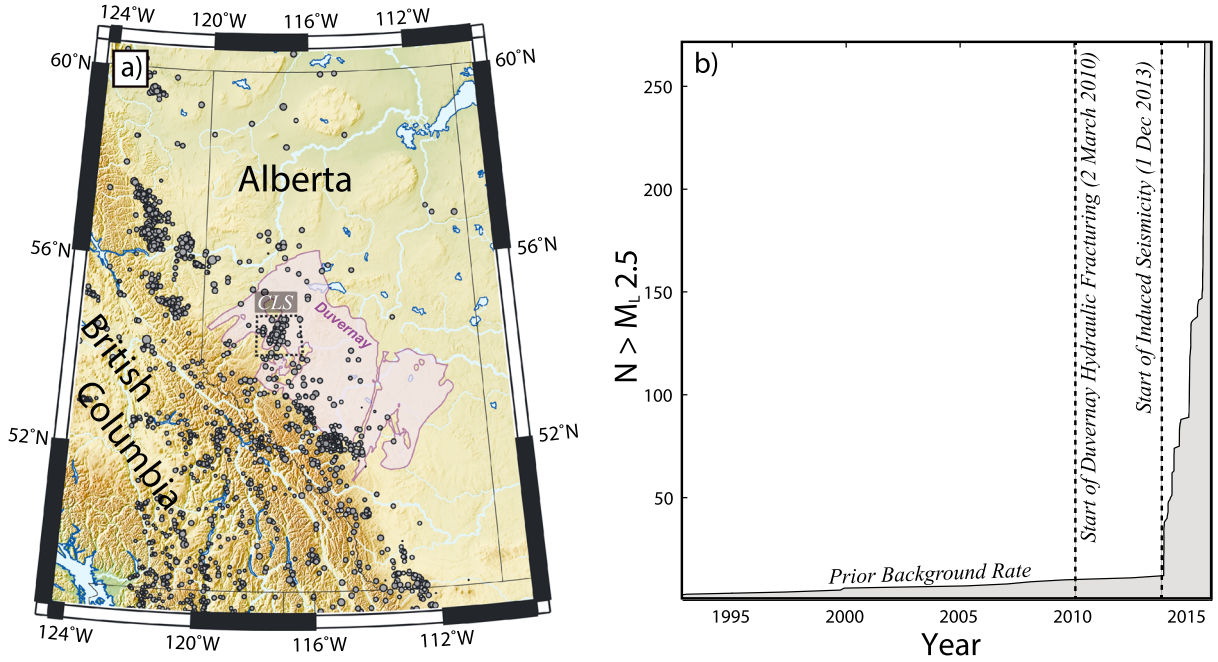

Figure 1. (a) Map placing the location of the CLS study area (dashed box) and Duvernay Formation (purple area) in geographic context to the Alberta Basin portion of the WCSB and the earthquakes therein (gray circles). (b) Cumulative number of earthquakes greater than magnitude 2.5 within 100 km of Crooked Lake. A marked increase in seismicity rate is observed as of 1 December 2013, coinciding with the first case of hydraulic fracturing-induced seismicity in the region.

Regional Alberta Observatory for Earthquake Studies Network (RAVEN) [*Alberta Geological Survey*, *AGS Canada*, 2013; *Schultz and Stern*, 2015]. In cases where clusters have supplemental local array data available, we are able to clearly delineate planar features trending from the stimulation interval into the Precambrian basement, using double-difference relocations. Our focal mechanism solutions favor an approximate N-S/E-W strike-slip motion.

2. The Duvernay Formation

The Upper Devonian (Frasnian) Duvernay Formation (Woodbend Group) is composed of multicyclic units of black organic-rich shale and bituminous carbonates [*Weissenberger and Potma*, 2001], ranging between 25 and 60 m in thickness [*Davis and Karlen*, 2013] and extends throughout most of central Alberta. The Duvernay Formation overlies the Cooking Lake Formation platform in the East Shale Basin, west of the Leduc Rimbey Meadowbrook reefal trend, and the Majeau Lake Formation in western central Alberta [*Stoakes*, 1980]. The Duvernay Formation shales are the basinal equivalent to the Leduc Formation reef [*Switzer et al*., 1994]. Overall, the Duvernay Formation exhibits a westward increase in thermal maturity from the immature to the gas-generation zone [*Rodgers*, 2014]. This hydrocarbon potential has been exploited successfully within Duvernay-sourced conventional oil and gas reservoirs including the surrounding Leduc Formation and underlying Swan Hills Formation carbonate buildups. Much of the Duvernay Formation in the area of optimal maturity is overpressured, with noted cases beyond gradients of 19 kPa/m in deep basin settings [*Davis and Karlen*, 2013; *Fox*, 2015]. Preliminary resource prospecting median estimates placed shale-hosted oil and natural gas liquid volumes at 61.7 and 11.3 billion barrels, respectively [*Rokosh et al*., 2012].

Development of the Duvernay shale-hosted hydrocarbon resources has become economically feasible in recent years [*Rodgers*, 2014], with unconventional operations in the Fox Creek region beginning in June 2010. To date there have been more than 290 horizontal well completions occurring in the Duvernay Formation between 2.6 and 4.0 km depth in the Fox Creek area. The typical number of perforations per stage, stages per well, and wells per pad range between 1–8, 13–42, and 1–8, respectively, for completions that appear to be seismogenic. Average mean pressures, pumping rates, total pumped fluid volume, and proppant weight in well for individual stages are 62.6 MPa, 9.4 m^3/min, 1200 m^3, and 240 t, respectively.

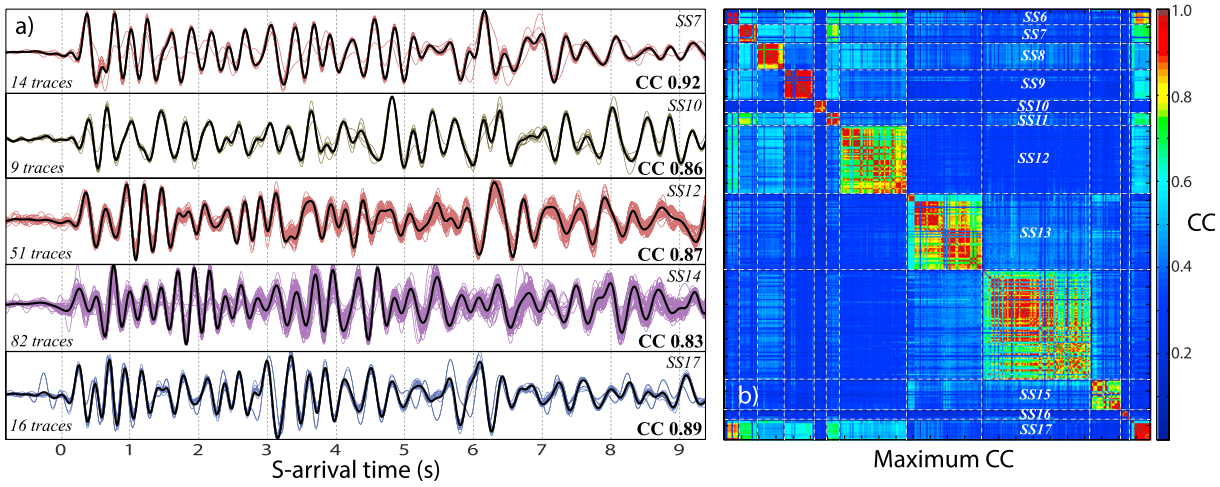

Figure 2. (a) Beam-averaged trace (black line) of individually stacked waveforms (colored lines) on BRLDA.HHE starting at roughly the *S* arrival times for multiple distinct sequences filtered between 1 and 5 Hz. Superimposed text provides details on traces count, sequence ID, and averaged correlation coefficient (CC) to the beam average. (b) Waveform similarity plot. Earthquakes since the onset of induced seismicity continue to be highly correlated in their waveform characteristics. The scale bar on the right indicates the degree of waveform similarity via the CC. Distinct sequences have been binned and labeled for further reference.

3. Earthquake Clustering

Seismicity within the study region has increased in earthquake rate starting on 1 December 2013 (Figure 1b). Originally, these earthquakes were called the Crooked Lake Sequences (CLS) in reference to the nearby lake ~30 km west of Fox Creek around where the epicenters initially clustered. For simplicity we will continue to use the CLS/SSX abbreviations in this paper. Furthermore, these earthquakes were divided into five seismically distinct sequences based on waveform similarity and temporal clustering (SS1–SS5). Since 2014, these earthquake sequences have become increasingly prolific and pervasive, expanding into the wider Fox Creek area.

In a previous study, *Schultz et al*. [2015a] showed that the CLS contain strong waveform similarities for sequences from December 2013 to the end of 2014. Following the same methodology as in *Schultz et al*. [2015a], we repeat our waveform similarity analysis for all events starting on 1 January 2015 through February 2016. We compare waveform similarity using interevent cross correlations [*Reyes and West*, 2011] on the east component of the nearby BRLDA station filtered from 1 to 5 Hz (Figures 2a and S1 in the supporting information). BRLDA is recorded using a broadband Trillium Compact seismometer sampled at 100 Hz [*AGS*, 2013]. This selection of frequency band, station, and channel was chosen to maximize the signal-to-noise ratio, providing the clearest view of the waveforms. The earthquake-station paths for most cluster locations roughly maximize *S* wave arrival energy on the BRLDA.HHE channel, according to our focal mechanism determinations. The results of this updated analysis (Figure 2b) corroborate the previous finding: the CLS events continue to share a high degree of waveform similarity, sorting into discrete sequences. Using the current network detection thresholds, we have identified at least 12 new sequences (SS6–SS17) in addition to the original 5 (SS1–SS5). Average correlation coefficients (CCs) for events within a sequence (intrasequence) are as high as 0.90 for SS6–SS11. Furthermore, intersequence correlations (waveform similarities between sequences) often exceed 0.60, sometimes surpassing 0.80 (e.g., SS6 × SS17 and SS7 × SS11). On the other hand, we note considerable complexities in some sequence groupings (but still have CCs $>$0.50), possibly indicating the potential for further subdivision (e.g., SS12–SS15 on Figure 2b). The sequences identified by the clustering analysis also reveal that distinct sequences are separated temporally.

4. Temporal Relationships

Earthquake catalogues are routinely processed at the Alberta Geological Survey [*Stern et al*., 2013; *Schultz et al*., 2015c] using data from nearby regional seismic networks [e.g., *Gu et al*., 2011; *AGS*, 2013; *Eaton*, 2014] and regionally calibrated velocity models [e.g., *Schultz et al*., 2015a]. Moment magnitudes are

determined both from moment tensor inversions and pseudo acceleration amplitudes [*Atkinson et al*., 2014; *Wang et al*., 2016]; the largest Fox Creek events to date are M ~4 (23 January 2015 SS6, 13 June 2015 SS10, and 12 January 2016 SS17).

The temporal characteristics of clustering observed at the CLS were further examined using a multichannel, cross-correlation detection method [*Schaff*, 2008] to increase the number of detected events. The 17 templates used in the search algorithm are based on beam-averaged waveforms from each uniquely identified sequence. The detection search is conducted over a time window beginning at least 1 month prior to the first recorded event or the first stimulation interval at the purported well pad, whichever is earlier. The time window ends 6 months after the last stimulation or 1 month after the last recorded event (including newly detected events), whichever is later. The CC detection threshold is set at 0.30 to ensure negligible probability of false alarms [*Schaff*, 2008]. The absence of detections before initial stimulation in all sequences (except at SS15, discussed in section 5.1) further suggests that our choice of CC threshold mitigates false detections.

The application of the cross-correlation detector roughly quadruples the size of our event catalogue, to ~2000 earthquakes. The extended catalogue depicts a clustering of sequences in time (Figure 3a); the reduction in the magnitude of completeness with the installation of RAVEN is also apparent (e.g., increase in events within and after SS6). In some sequences, we observe a sharp transition from quiescence to increased earthquake rates during a period coincident with nearby hydraulic fracturing operations (Figures 3b and S2). For the SS11 case, we observe that the first recorded earthquakes lag the closest hydraulic fracturing stage by 4 to 8 h. In many sequences, it appears that the earthquake rate progresses into a second phase of reduced intensity, often timed with the cessation of stimulation (Figures 3b, 3c, and S2). This second phase can continue for up to 3 months after hydraulic fracturing stimulation ends. In some cases, the largest-magnitude events are observed during this posttreatment period (e.g., SS6, SS10, and SS17 in Figures 3a and S2).

We also observe a case (SS15) in which the seismicity occurs in two distinct time periods. The first period of seismicity is brief, and it is recorded during the tail end of stimulation at an adjacent well pad (Figure 3c). The second period features the previously described pattern of high seismic activity during the stimulation phase of the closest well pad, followed by diminished seismic activity during the shut-in phase of this well. This pattern suggests that the propensity for induced seismicity at this location was apparent, based on stimulation of a neighboring well, before the treatment at the closest well pad began.

Lastly, we explore the relationship between cumulative seismic moment versus total injected volume [*McGarr*, 2014], in addition to cumulative number of events versus total injected volume [*Shapiro et al*., 2007, 2010]. We analyze SS11 for this investigation due to its simplicity (related to a single well pad) and the relatively brief temporal clustering of earthquakes. We consider the volume following event initiation, which occurred during the sixth stage. Furthermore, for these analyses we assume a constant b value due to inadequate catalogue completeness to rigorously test temporal variations. Also, no fluid flow back is assumed due to lack of reports of if, when, and how much flow back occurred. The regression of these relationships (Figure 4) shows a linear trend for both the cumulative seismic moment (R^2 of 0.985) and total earthquake count plots (R^2 of 0.762). The clear trends support the conclusion that the activity is occurring in direct response to the injection program [e.g., *Kwiatek et al*., 2015].

5. Spatial Distribution of Induced Seismicity Near Fox Creek

The observed similarity of earthquake waveforms within sequences implies spatial clustering of earthquakes. To validate this claim, we refine the hypocentral locations with HypoDD [*Waldhauser and Ellsworth*, 2000], as applied to the publicly available, regional waveform data [*AGS*, 2013; *Stern et al*., 2013; *Schultz et al*., 2015c]. The input regional velocity model [*Schultz et al*., 2015a] was based on information from sonic well logs for the shallow sedimentary sections. For the crystalline basement and upper mantle, the velocity model was based on information from receiver functions [*Chen et al*., 2015] and CRUST1.0 model [*Laske et al*., 2013]. A starting focal depth of 3 km is chosen based on the approximate depth of hydraulic fracturing operations. To ensure the robustness and stability of our results, we apply a bootstrap approach [*Efron and Tibshirani*, 1986] that randomly removes 90% of the input earthquakes before each of the 1000 trial inversions. We define robust hypocenter parameters as the modal value measured from the statistical distributions which are well behaved (e.g., are not multimodal). Analogously, variances in hypocentral parameters are estimated from the standard deviation of the statistical distributions.

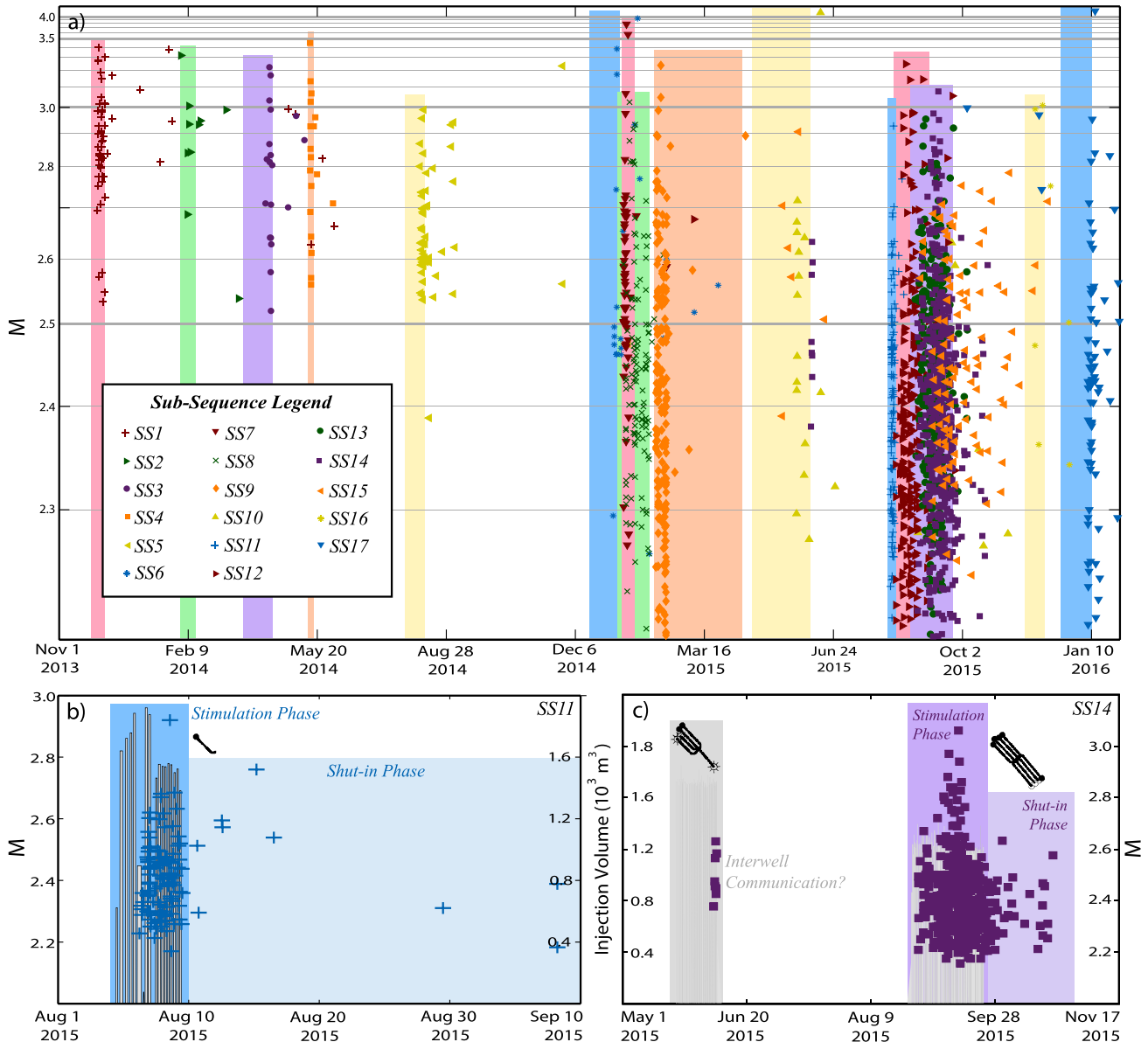

Figure 3. (a) Timing and scaled magnitudes [*Agnew*, 2015] of earthquakes near Fox Creek using conventionally located catalogues and additional detections from cross-correlation detection methods. Distinct earthquake clusters are denoted according to unique identifiers in the plot legend. For comparison the timing of hydraulic fracturing stimulation operations at wells nearest to each cluster are depicted with a color-coded area. (b) Analogous plot to the top plot but filtered to include only SS11 relevant data. The additional gray bars depict the timing of stimulation volumes; the black "tadpoles" depict the shape of well pad trajectory; and finally, the shaded areas represent the changes in earthquake cluster rates and well shut-in. (c) Similar to Figure 3b with additional denotations for suggested interwell communication.

Our double-difference inversions provide more than 250 robust event hypocenters from the CLS (Figure 5). Overall, the locations are well constrained, with epicentral variances on the order of 1 km (a value smaller than the typical lateral extent of a single well pad). On average, we obtain focal depths in the range of ~5 ± 2 km, with depth errors on the order of 2 km. The relocated events of the CLS sequences cluster about their temporally associated well (Figure 5). In almost all sequences, the cluster centroid is within the location error of its purported well (based on timing). An exception is the SS5 cluster, which is on average 4 km from the purported well; it is uncertain whether this distance from the well is simply a processing artifact or truly indicative of the location of the induced seismicity cluster. Within some of the clusters, there is an apparent alignment of events along linear features. We hesitate to interpret these alignments as structures, because the location uncertainties of this regional data set are of the same order (or larger) than the expected fault

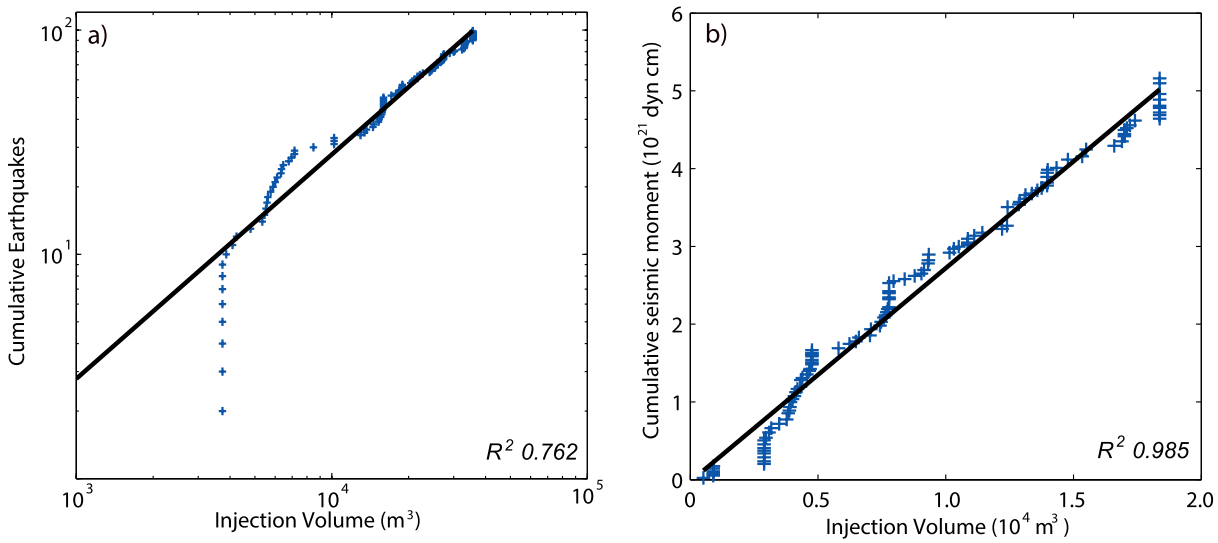

Figure 4. (a) Logarithmic comparison of cumulative number of earthquakes versus injection volume (blue crosses) and best linear fit to the data (black line). (b) Cumulative seismic moment versus injection volume (blue crosses) and best linear fit to the data (black line). In both plots the earthquake catalogue was filtered for SS11 and operational volumes are for all stages following the sixth, the stage on which earthquakes were first detected.

dimensions for events of this magnitude. Moreover, the lateral trends of epicenters align with the expected error ellipsoid orientation.

5.1. Red-Light Case Studies

In this section we focus on two sequences which triggered the red-light protocol in the study area [*AER*, 2015]. The first occurred on 13 June 2015, as part of SS10. It was initially reported as having a magnitude

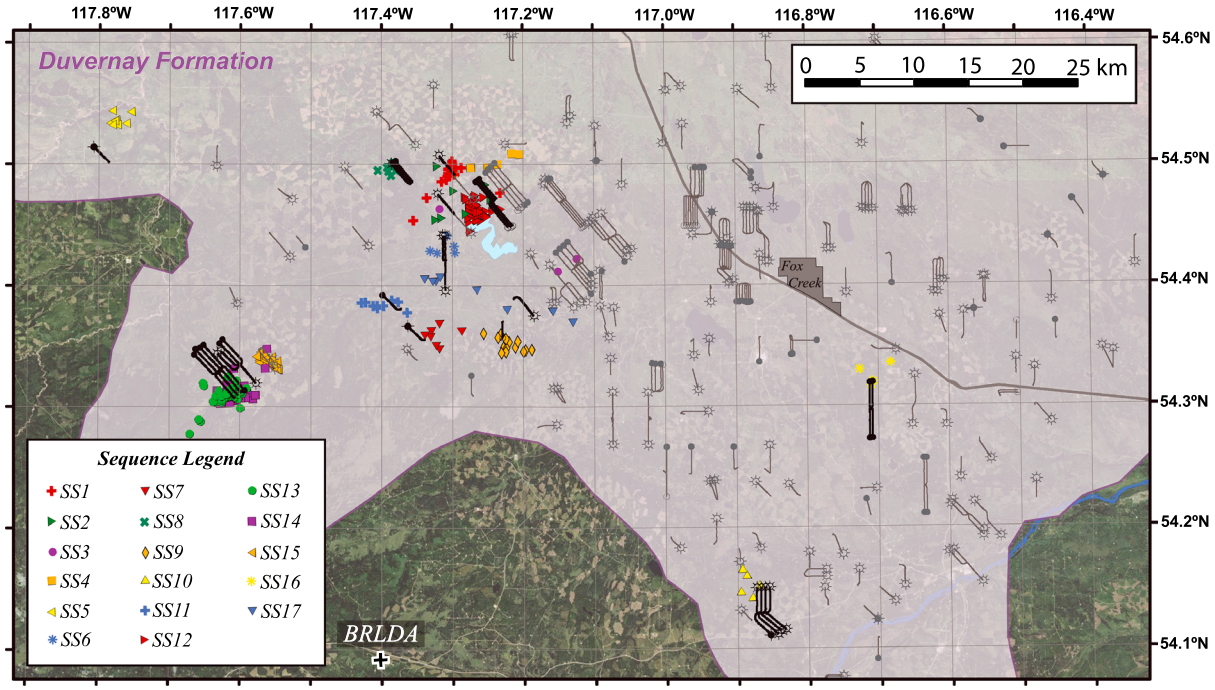

Figure 5. Map of double-difference relocated seismicity from public seismic networks in the study area. Earthquake cluster locations (see legend for symbols) are placed in geographic context to the Fox Creek town boundaries (dark gray area); Crooked Lake (blue area); the Duvernay Formation (purple area); horizontal completions in the Duvernay (black "tadpoles, i.e., circles and lines); and the nearby RAVEN station, BRLDA (black cross). Wells linked to seismic clusters have had their horizontal segments bold faced.

of 4.4 M_L, with the moment magnitude later reported as M 3.9 [*Wang et al*., 2016]. The second occurred on 12 January 2016 as part of SS17; the initial magnitude of 4.8 M_L was later revised to a value of M 4.1.

For the SS10 sequence, we have the benefit of eight additional surface stations that were installed by the operator in an approximately symmetric array within a radius of ~3 km from the surface well location (Figure 6a). Conventional detections and locations in this supplemented catalogue produce a rich data set having more than 200 events (M ~0.4–3.9) for the period from 29 April to 5 July in 2015. In comparison, the catalogue obtained for this sequence from regional cross-correlation detections contains only about 20 events. Based on waveform similarity, earthquakes within this sequence can be further subdivided into three distinct clusters; events within each of these three clusters have beam-average CCs of ~0.90. Only the NE cluster, which was responsible for the red-light event (red in Figure 6), was detected on publicly accessible, regional networks. We perform robust double-difference relocations for each of the three distinct clusters in SS10, using the same techniques described in the preceding section. This produces very well constrained event sets, with variances in hypocentral location of only about 20 m. Within these sets there is remarkable consistency: events are trending along ~N-S striking and subvertically oriented planar features that reside between the stimulation interval and the first few hundred meters of Precambrian basement. We note that the large majority of hypocenters are within the basal sedimentary succession. Furthermore, the NE cluster runs subparallel to the well trajectory, at an average separation distance of ~475 m. To determine hypocenter orientations more precisely, we perform weighted, plane fitting regressions. Only the largest NE cluster yields stable inversions for strike direction, which we determined to be 357° (or 177°) ±4°. This planar feature is between l and 2 km in observed strike length and 400–600 m in dip length.

In the second, more recent red-light case (SS17), there are additional operator-provided data for four local stations configured in a lightning-bolt shape (Figure 7a; furthest station is outside the area shown in the plot), with the furthest being ~7.5 km NE from the well surface location. Utilizing these additional data we are able to conventionally locate more than 90 earthquakes, of M 0.1–4.1, in comparison to the ~70 events that were detected using cross-correlation methods to the regional network data. Within the supplemented catalogue, we find that most events have a high degree of waveform similarity, with CCs of 0.75 to the cluster beam average. This high degree of similarity likely enabled the excellent performance of the cross-correlation-based detection algorithm. Again, double-difference relocations exhibit a high degree of agreement with the previous locations (Figure 7); hypocenters have a variance of ~15 m laterally and ~20 m vertically. The epicenters closely follow the southern well trajectory in an ~N-S trending orientation. In depth, events begin at the level of the Duvernay stimulation interval and extend downward into the shallow Precambrian basement. Most of the seismic events are within the first ~200 m below the wellbore trajectory. Regression of the locations to a plane suggests a strike angle of 7° (187°) ±35° with subvertical dip (Figure 7b). Overall, the extent of the trending hypocenters is approximately 0.5–1.0 km along the apparent strike length and 200–600 m along dip length. In both case studies the addition of downhole microseismic sensors would greatly improve the absolute positioning of the hypocenters.

6. Focal Mechanism Constraints

Focal mechanisms can be routinely determined from regional data for earthquakes of M 3.5 and greater but are a challenge for smaller events due to noise in the microseism band. Fortunately, for the CLS we can take advantage of the similarity of the earthquake waveforms to aid in constraining focal mechanism [e.g., *Vavryčuk*, 2015]. In particular, we align and stack traces to amplify the signal-to-noise ratio by factors up to $\sqrt{N}$, where N is the number of stacked traces. This extends the effective magnitude range over which we can determine moment tensors. For example, stacks with 25 traces can reduce the threshold by roughly half a magnitude unit. We may therefore apply the time domain waveform inversion method [*Dreger*, 2003] to smaller-magnitude events. This approach has been previously established in the Fox Creek region [*Wang et al*., 2016] for earthquakes with magnitude larger than 3, which are well recorded at low frequencies (0.08–0.4 Hz). For events with poor signal-to-noise ratio, we resort to a double-couple grid search using data only from the closest station BRLDA in a bandwidth of 0.4–0.9 Hz. We refer the reader to *Wang et al*. [2016] for more information on the workflow, sensitivity tests, variance, and stability of moment tensor inversions within the Fox Creek area.

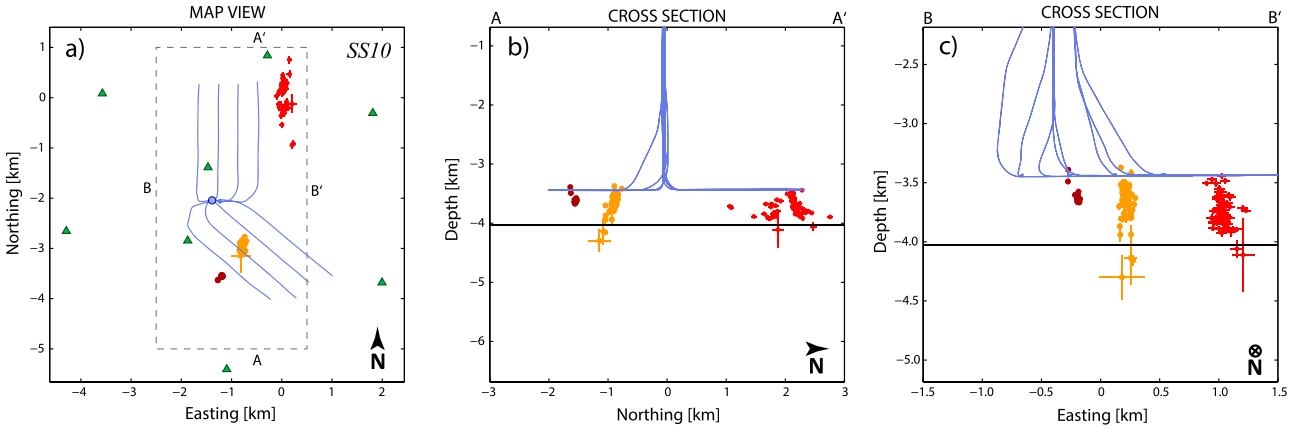

Figure 6. Double-difference relocations of earthquake locations with supplemental industry data for SS10. (a) Map view of earthquake locations (crimson hue circles) and their variance to two standard errors (crosshairs) in relation to recording stations utilized in relocation (green triangles), the well surface location (blue circle), and well trajectory (blue lines). The boundaries of depth cross sections are denoted by the lateral extent of the dashed box. (b) Depth cross section trending S-N. (c) Cross section trending W-E; in both cross sections the depth to Precambrian basement is indicated via a horizontal black line. In all plots the earthquakes locations have been distinguished in color to clearly differentiate clustering.

Four of the CLS sequences can be inverted to determine full moment tensor solutions (SS6, SS7, SS10, and SS17) with excellent waveform fit (Figures S3 and S4). For these sequences, we find predominantly double-couple solutions, in accordance with previous studies [*Wang et al.*, 2016]. In fact, we obtain double-couple components as high as 98% and no smaller than 70%.

The finding of predominantly double-couple components provides justification for utilizing a double-couple grid search on remaining sequences. This double-couple search procedure was successful for four additional sequences (SS8, SS9, SS11, and SS12). Within our entire tensor library, the largest contributor to double-couple fault motion is strike slip (Figure 8). For example, our fully inverted moment tensors exhibit strike-slip components no smaller than 90%, while our grid-searched solutions range between 55 and 88%. In almost all determinable solutions, focal mechanisms share a roughly N-S/E-W orientation. For the overall *P* axis vector, within the fully inverted subset we determine an average azimuth of $45° \pm 5°$ and $61° \pm 12°$ for the grid-searched solutions.

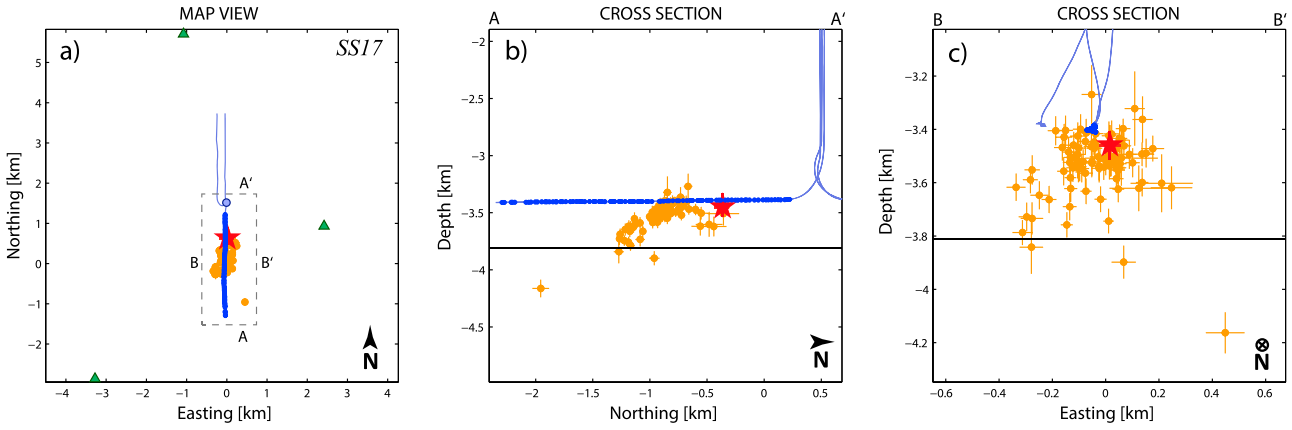

Figure 7. Analogous plot to Figure 4, double-difference relocations of earthquake locations with supplemental industry data for SS17. (a) Map view of earthquake locations (orange circles) and their variance to two standard errors (crosshairs) in relation to recording stations utilized in relocations (green triangles), the well surface location (blue circle), and well trajectory (blue lines). The boundaries of depth cross sections are denoted by the lateral extent of the dashed box. (b) Depth cross section trending S-N. (c) Cross section trending W-E; in both cross sections the depth to Precambrian basement is indicated via a horizontal black line. In all plots the location of the *M* 4.1 earthquake is denoted as a red star.

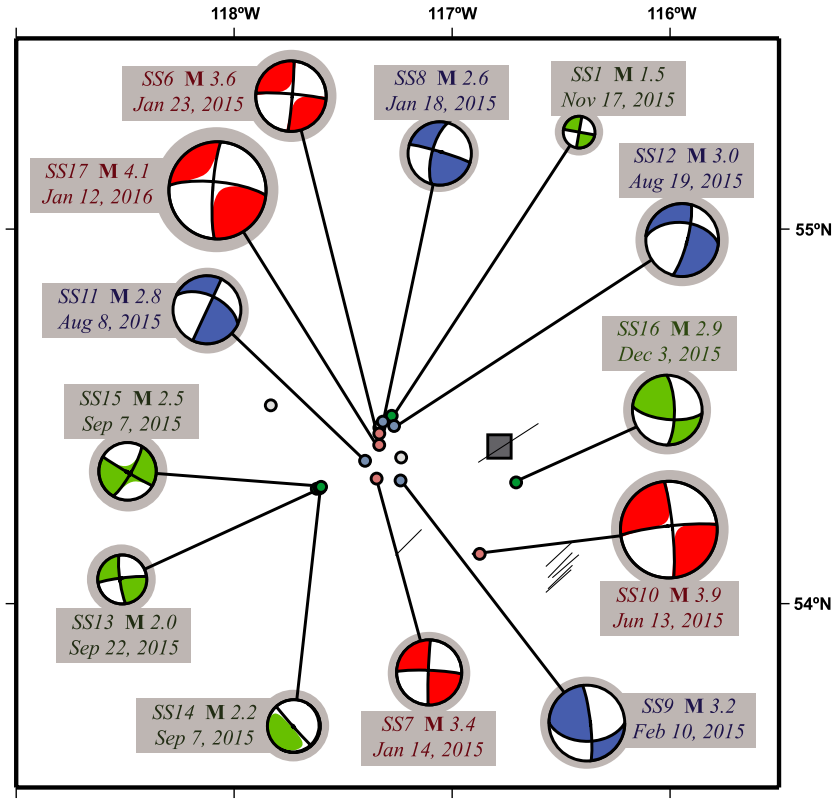

Figure 8. All determinable moment tensors for the CLS clusters. Inverted (red), double-couple grid searched (blue), and industry-donated (green) beach balls are compared to their centroid locations (circles), Fox Creek (gray square), and maximum horizontal stress direction from wellbore breakouts (~45° lines) [*Reiter et al.*, 2014]. The text insets describe the parent event from which the corresponding focal mechanism results were stacked and derived.

7. Discussion

Within the WCSB it has been demonstrated that regional changes in earthquake rate correlate to hydraulic fracturing operations in the WCSB [*Atkinson et al.*, 2016]. In fact, the earthquakes experienced in the CLS region are some of the largest to be associated with hydraulic fracturing globally. Thus, a better understanding of the nature of these events is crucial in assessing the potential change in seismic hazard near Fox Creek.

Our findings address the first three indicators in the classic criteria for distinguishing induced seismicity [*Davis and Frohlich*, 1993]: (1) is there an apparent change in rate of seismicity, (2) is the rate change correlated with suspect operations, and (3) is there an applicable spatial correspondence? In the case of the CLS near Fox Creek we have demonstrated an obvious change in rate (Figure 1b) that is not related to improvements to the recording networks [*Schultz et al.*, 2015c; *Cui and Atkinson*, 2016]. At present the delay between initial Duvernay development and first induced earthquake in the Fox Creek region is of note (Figure 1b); currently, it is not understood why only certain wells are apparently seismogenic. Potential explanations could be related to geological, hydrological, tectonic, or operational controls on the susceptibility to seismicity at a regional scale. However, when we consider only Duvernay completions proximal to sequences, a strong temporal correlation with a high degree of confidence is observed even for just the first four sequences [*Schultz et al.*, 2015a]. With additional data (SS6–SS17), we find that the CLS continues to be transient and timed with the proximal Duvernay completions (Figures 3 and S2). Among these clusters, we highlighted two sequences (SS11 and SS15) to demonstrate the apparent two-phased nature of the earthquake rates in this region (Figures 3b and 3c): higher seismic activity during stimulation periods followed by lower and gradually diminishing seismic rate during well shut-in. A further analysis demonstrates that seismic observables from the SS11 cluster can be associated with stimulation volumes to a high degree of agreement (Figure 4). Lastly, our double-difference relocations of the CLS indicate that close epicentral association with the suspected operations (Figure 5) and at depths (5 ± 2 km) are consistent with other induced seismicity in

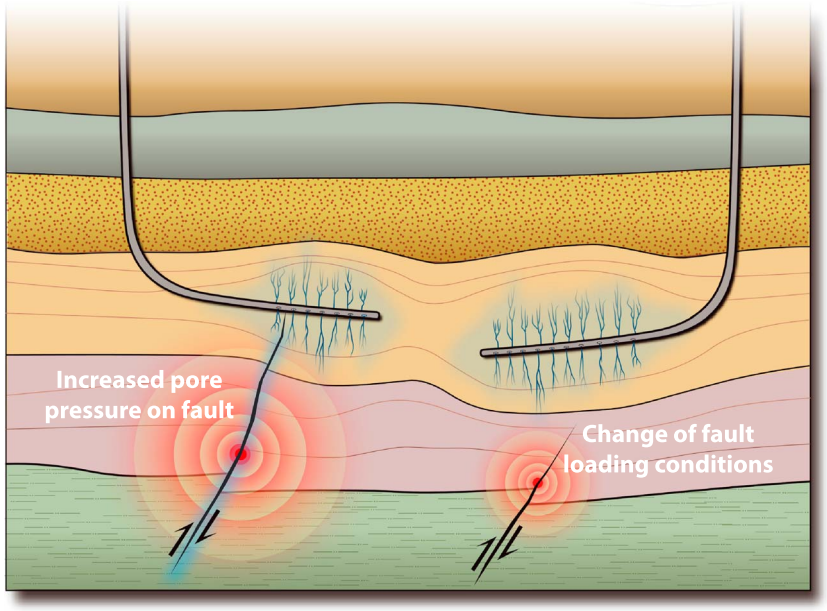

Figure 9. Conceptual diagram which explores two physical mechanisms of initiating slip on a fault as a consequence of hydraulic fracturing. In the left-hand scenario stimulated fracture growth provides hydraulic communication with a pre-existing fault. In this case, increased pore pressure on the fault during stage stimulation initiates the fault slip. In the right-hand scenario the lateral extent of the completed well is hydraulically isolated from the fault. However, slip can still be initiated on this fault due to stress perturbations associated with mass/volume flux. These perturbations are transmitted poroelastically, during both stimulation and production phases of the well life cycle.

the WCSB [*Zhang et al*., 2016]. Overall, the continued spatiotemporal association of the CLS with Duvernay completions greatly increases our confidence in the induced nature of these earthquakes.

We also note that the CLS earthquakes tend to cluster into distinguishable sequences or swarms (Figure 2), which have been argued as a characteristic of induced seismicity in general [*Skoumal et al*., 2015a, 2015b]. We interpret the swarminess in the CLS as a consequence of repeatedly stimulating the same fault to failure conditions [*Goertz-Allmann and Wiemer*, 2013] via pore pressure increase [*Kummerow et al*., 2014] during fluid injection into overpressured, low-permeability rocks [*Cox*, 2016]. In this sense, intrasequence differences in waveform similarity (Figure 2b) can be viewed as a result of hypocentral variation along fault patch areas, en echelon faulting, subtle changes in focal mechanism orientation, and/or complexity in the fault network [*Got and Fréchet*, 1993].

Often, induced seismicity is geomechanically explained via anthropogenic alteration of the ambient stress field that promotes failure on optimally oriented preexisting faults [*Raleigh et al*., 1976]. For injection-related induced seismicity, two potential triggering mechanisms are considered [*Segall and Lu*, 2015]. First, there may be direct hydraulic communication between stimulated fractures and the preexisting fault; increasing pore pressure on this fault hydraulically opens it, allowing shearing stress to surpass fault friction and cohesion (Figure 9, left side). Alternatively, the stimulated fractures and preexisting fault may be hydraulically isolated; in this case, perturbations in the stress field due to increases/decreases in mass or volume are transmitted to the nearby fault poroelastically (Figure 9, right side).

Within the Fox Creek area, our moment tensor inversions place constraints on the orientations of preexisting faults. In general, focal mechanisms suggest strike-slip motion on subvertical, ~N-S/E-W oriented faults in almost all sequence cases (Figure 8). This is in accordance with information on the regional ambient stress field which suggests that the Fox Creek region is in a strike-slip regime [*Reiter and Heidbach*, 2014; *Fox*, 2015], oriented at ~45° [*Reiter et al*., 2014]. The consistency between stress considerations and our results for both the average *P* axis orientation ($45° \pm 5°$ and $61° \pm 12°$) and slip type suggests a high level of fidelity in our inversion determinations. Moreover, geomechanical stress considerations have also suggested N-S as the preferred fault plane orientation [*Murray*, 2016]. For two clusters (SS10 and SS17), dense-array double-difference relocations corroborate the sense of slip as N-S dextral motion (Figures 6 and 7), similar to the

findings of *Bao and Eaton* [2016] for SS6. In the NE cluster of SS10, we observe subvertical faults with strike orientations of 357° ± 4°, which is within the error range of other reported focal mechanism determinations (354° ± 1°) [*Wang et al*., 2016]. Similarly, orientations determined for the subvertical fault in SS17 suggest an azimuth of 187° ± 35° in comparison to the focal mechanism strike of 184° ± 3°. Furthermore, the expected fault radius (~1 km) based on the event magnitudes and stress drops [e.g., *Yenier et al*., 2016; *Clerc et al*., 2016] is consistent with the activated area of hypocenters observed from the two red-light events.

These orientations have implications for understanding the Devonian and pre-Devonian structures in the WCSB. It has been suggested that the basement rocks in much of the CLS region have experienced transtensional/extensional tectonism in the geologic past, and structures associated with the basement continue up into the overlying Devonian sedimentary succession [*Berger and Davies*, 1999; *Davies and Smith*, 2006]. In addition, high-angle fractures, polished slip faces, and associated cleavage observed in drill core have been interpreted as naturally occurring subvertical fractures irregularly distributed throughout the Duvernay [*Soltanzadeh et al*., 2015]. Furthermore, structural features within basal sedimentary successions have been suggested by previous authors [*Davies and Smith*, 2006] as the preferred sites for upward flow of hydrothermal fluids. In the area of Fox Creek, linear dolomite bodies in the Swan Hills Formation (underlies the Duvernay in CLS region) platform and reefal margins are attributed to upward flow of hydrothermal fluids along subvertical faults [*Duggan et al*., 2001; *Green and Mountjoy*, 2005]. These geological features appear to have had a measurable effect on the spatial distribution of induced seismicity, as induced earthquakes in central Alberta have shown an apparent trend along the margins of the Swan Hills Formation [*Schultz et al*., 2016].

In light of the presence of hydrothermal dolomite, which suggests vertical fluid flow via fault-related conduits in the geologic past [*Green and Mountjoy*, 2005; *Davies and Smith*, 2006], we argue that the triggering method in the CLS region is predominantly controlled by increased pore pressure communicated hydraulically (left-hand scenario in Figure 9). This conjecture is supported by the double-difference relocations of SS10 and SS17, indicating near-direct contact between the preexisting fault and well trajectories (Figures 6 and 7). Our results suggest that increased pore pressure resulting from Duvernay stimulation is rapidly communicated along the damage zone of mechanically active faults, until reaching a zone of fault weakness [e.g., *Zhang et al*., 2013; *Hornbach et al*., 2015]. Furthermore, during the hydraulic fracturing process pore pressure is stimulated beyond the minimum stress gradient, propagating tensile failures throughout the target rock [*King*, 2010]. These fractures can grow to lengths of up to 500 m vertically [*Davies et al*., 2012], allowing for plausible hydraulic communication at the average distances observed in the CLS (see NE cluster in Figures 6a and 5). On the other hand, supplemental information on fracture growth lengths specific to the Duvernay completions would help to more confidently assert pressure transport mechanisms. For example, the SS5 cluster is located at the greatest distance from its adjacent well (~4 km). While previous case studies have noted hydraulic fracturing-related seismicity at similar lateral offsets [*Holland*, 2013], the exact triggering mechanism in these cases has remained unclear. Additional, high-resolution case studies would aid in the interpretation of such cases (e.g., *Bao and Eaton* [2016] for SS6–SS9).

While we have argued that pore pressure is the first-order triggering effect for CLS-induced seismicity, we also note the potential for second-order triggering effects. The most noteworthy is the SS15 cluster, which was observed to trigger initially with completions at an adjacent well, before undergoing seismicity during the completion of the nearest well (Figures 3c and 5). In this case it remains plausible that the adjacent hydraulic fracturing operations have perturbed the ambient stress field [e.g., *Martínez-Garzón et al*., 2013; *Schoenball et al*., 2014], causing the initial fault slip at greater distance. This interpretation is particularly attractive, as sequences SS14 and SS15 (Figures 5 and 8) both suggest focal mechanisms which are nonoptimal for reactivation in the regional stress field. However, in these cases we note that discerning relative contributions from poroelastic stress transmission and hydraulic communication via pore pressure perturbation would require further geomechanical analysis [e.g., *Deng et al*., 2016].

8. Conclusions

From our analyses of the CLS seismicity near Fox Creek, we reach the following conclusions:

1. Since 1 December 2013, there has been a pronounced increase in the rate of seismicity in the Fox Creek region related to nearby hydraulic fracturing completions in the Duvernay Formation. The first case of induced seismicity lags the first horizontal hydraulic fracturing well by almost 3 years.

2. The CLS seismicity can be separated into transient clusters in time, space, and focal mechanism. This clustering of earthquakes is interpreted as a consequence of repeated stimulation of the same fault to failure via pore pressure increase during hydraulic fracturing operations into overpressured, low-permeability rocks.
3. Focal mechanism solutions are predominantly strike-slip motion on ~NS/EW striking, subvertical faults. These slips are consistent with the ambient stress field.
4. Imaging of hypocenters on local, dense arrays suggests ~N-S trending subvertical faults from the Duvernay Formation down to the shallow Precambrian basement. These fault orientations are consistent with prior work suggesting transtensional/extensional tectonic environment in the geologic past. These preexisting faults have then undergone anthropogenic reactivation as strike slip in the current regional stress field.
5. In the red-light cases (SS10 and SS17), direct hydraulic communication between the stimulated well and imaged faults is suggested. We interpret pore pressure increase as the dominant (first-order) initiation factor for these sequences.
6. Additional cases have been noted, which suggest potential second-order effects including activation at distance (up to 5 km, e.g., SS5), interwell communication (SS15), or fault slip motion activated at nonoptimal orientations in the current stress field (SS14 and SS15). We interpret these findings as potentially suggestive of stress perturbations transmitted poroelastically; however, their effect at distance will require further geomechanical inquiries.

Acknowledgments
We would like to thank two anonymous reviewers for their comments in improving this manuscript. Regional seismic waveform data utilized in this study [*AGS*, 2013] are publicly available through the Incorporated Research Institutions for Seismology Data Management Centre. Supplemental seismic waveform data and hydraulic fracturing tour reports were provided from industry through the Alberta Energy Regulator. Additional focal mechanisms were donated anonymously from industry in support of this work. We acknowledge the financial support of the Natural Sciences and Engineering Research Council for the induced seismicity research in Canada.

References

Agnew, D. C. (2015), Equalized plot scales for exploring seismicity data, *Seismol. Res. Lett.*, *86*(5), 1412–1423, doi:10.1785/0220150054.
Alberta Energy Regulator (2015), Subsurface order no. 2: Monitoring and reporting of seismicity in the vicinity of hydraulic fracturing operations in the Duvernay zone, Fox Creek, Alberta. AER Bulletin 2015–07, 3 pp. [Available at https://aer.ca/documents/orders/subsurface-orders/SO2.pdf.]
Alberta Geological Survey (AGS Canada) (2013), Regional Alberta Observatory for Earthquake Studies Network. International Federation of Digital Seismograph Networks. Other/Seismic Network. doi:10.7914/SN/RV.
Atkinson, G., K., Assatourians, B. Cheadle, and W. Greig (2015), Ground motions from three recent earthquakes in western Alberta and northeastern British Columbia and their implications for induced-seismicity hazard in eastern regions, *Seismol. Res. Lett.*, *86*(3), doi:10.1785/0220140195.
Atkinson, G. M., D. W. Greig, and E. Yenier (2014), Estimation of moment magnitude (M) for small events ($M < 4$) on local networks, *Seismol. Res. Lett.*, *85*(5), 1116–1124, doi:10.1785/0220130180.
Atkinson, G. M., et al. (2016), Hydraulic fracturing and seismicity in the Western Canada Sedimentary Basin, *Seismol. Res. Lett.*, *87*(3), doi:10.1785/0220150263.
Babaie Mahani, A., R. Schultz, H. Kao, D. Walker, J. Johnson, and C. Salas (2016), Fluid injection and seismic activity in the northern Montney Play, British Columbia, Canada, with special reference to the 17 August 2015 M_w 4.6 induced earthquake, *Bull. Seismol. Soc. Am.*, in press.
Bao, X., and D. W. Eaton (2016), Fault activation by hydraulic fracturing in western Canada, *Science*, doi:10.1126/science.aag2583.
Baranova, V., A. Mustaqeem, and S. Bell (1999), A model for induced seismicity caused by hydrocarbon production in the Western Canada Sedimentary Basin, *Can. J. Earth Sci.*, *36*(1), 47–64, doi:10.1139/e98-080.
BC Oil and Gas Commission (2012), Investigation of observed seismicity in the Horn River Basin. 29 pp. [Available at https://www.bcogc.ca/node/8046/download.]
Berger, Z., and G. R. Davies (1999), The development of linear hydrothermal dolomite (HTD) reservoir facies along wrench or strike slip fault systems in the Western Canada Sedimentary Basin, *Can. Soc. Petrol. Geol. Reserv.*, *26*(1), 34–38.
Chen, Y., Y. J. Gu, R. M. Dokht, and M. D. Sacchi (2015), Crustal imprints of Precambrian orogenesis in western Laurentia, *J. Geophys. Res. Solid Earth*, *120*, 6993–7012, doi:10.1002/2014JB011353.
Clarke, H., L. Eisner, P. Styles, and P. Turner (2014), Felt seismicity associated with shale gas hydraulic fracturing: The first documented example in Europe, *Geophys. Res. Lett.*, *41*, 8308–8314, doi:10.1002/2014GL062047.
Clerc, F., R. M. Harrington, Y. Liu, and Y. J. Gu (2016), Stress drop estimates and hypocenter relocations of induced seismicity near Crooked Lake, Alberta, *Geophys. Res. Lett.*, *43*, 6942–6951, doi:10.1002/2016GL069800.
Cox, S. F. (2016), Injection-driven swarm seismicity and permeability enhancement: Implications for the dynamics of hydrothermal ore systems in high fluid-flux, overpressured faulting regimes—An invited paper, *Econ. Geol.*, *111*(3), 559–587, doi:10.2113/econgeo.111.3.559.
Cui, L., and G. M. Atkinson (2016), Spatiotemporal variations in the completeness magnitude of the Composite Alberta Seismicity Catalog (CASC), *Seismol. Res. Lett.*, *87*(4), 853–863, doi:10.1785/0220150268.
Davies, G. R., and L. B. Smith Jr. (2006), Structurally controlled hydrothermal dolomite reservoir facies: An overview, *AAPG Bull.*, *90*(11), 1641–1690, doi:10.1306/05220605164.
Davies, R., G. Foulger, A. Bindley, and P. Styles (2013), Induced seismicity and hydraulic fracturing for the recovery of hydrocarbons, *Mar. Pet. Geol.*, *45*, 171–185, doi:10.1016/j.marpetgeo.2013.03.016.
Davies, R. J., S. A. Mathias, J. Moss, S. Hustoft, and L. Newport (2012), Hydraulic fractures: How far can they go?, *Mar. Pet. Geol.*, *37*(1), 1–6, doi:10.1016/j.marpetgeo.2012.04.001.
Davis, M., and G. Karlen (2013), A regional assessment of the Duvernay Formation; a world-class liquids-rich shale play, *GeoConvention 2013: Integration, Calgary*, 6–10.
Davis, S. D., and C. Frohlich (1993), Did (or will) fluid injection cause earthquakes?—Criteria for a rational assessment, *Seismol. Res. Lett.*, *64*(3–4), 207–224, doi:10.1785/gssrl.64.3-4.207.
Deng, K., Y. Liu, and R. M. Harrington (2016), Poroelastic stress triggering of the December 2013 Crooked Lake, Alberta, induced seismicity sequence, *Geophys. Res. Lett.*, *43*, 8482–8491, doi:10.1002/2016GL070421.

Dreger, D. S. (2003), TDMT_INV: Time Domain seismic Moment Tensor INVersion, in *International Handbook of Earthquake Engineering Seismology*, vol. 81B, pp. 1627, Acad. Press, London, U. K.
Duggan, J. P., E. W. Mountjoy, and L. D. Stasiuk (2001), Fault controlled dolomitization at Swan Hills Simonette oil field (Devonian), deep basin west central Alberta, Canada, *Sedimentology*, *48*(2), 301–323, doi:10.1046/j.1365-3091.2001.00364.x.
Eaton, D. (2014), Alberta Telemetered Seismograph Network (ATSN): Real-time monitoring of seismicity in northern Alberta, *CSEG Recorder*, *39*(3), 30–33.
Efron, B., and R. Tibshirani (1986), Bootstrap methods for standard errors, confidence intervals, and other measures of statistical accuracy, *Stat. Sci.*, 54–75, doi:10.1214/ss/1177013815.
Fox, A. (2015), A regional geomechanical study of the Duvernay Formation in Alberta, Canada. *GeoConvention 2015*: *New Horizon*, Calgary, Alberta, May 4–8.
Friberg, P. A., G. M. Besana-Ostman, and I. Dricker (2014), Characterization of an earthquake sequence triggered by hydraulic fracturing in Harrison County, Ohio, *Seismol. Res. Lett.*, *85*(2), 462, doi:10.1785/0220140127.
Goertz-Allmann, B. P., and S. Wiemer (2013), Geomechanical modeling of induced seismicity source parameters and implications for seismic hazard assessment, *Geophysics*, *78*, KS25–KS39, doi:10.1190/geo2012-0102.1.
Got, J. L., and J. Fréchet (1993), Origins of amplitude variations in seismic doublets: Source or attenuation process?, *Geophys. J. Int.*, *114*(2), 325–340, doi:10.1111/j.1365-246X.1993.tb03921.
Green, D. G., and E. W. Mountjoy (2005), Fault and conduit controlled burial dolomitization of the Devonian west-central Alberta Deep Basin, *Bull. Can. Pet. Geol.*, *53*(2), 101–129, doi:10.2113/53.2.101.
Gu, Y. J., A. Okeler, L. Shen, and S. Contenti (2011), The Canadian Rockies and Alberta Network (CRANE): New constraints on the Rockies and Western Canada Sedimentary Basin, *Seismol. Res. Lett.*, *82*, 575–588, doi:10.1785/gssrl.82.4.575.
Holland, A. A. (2013), Earthquakes triggered by hydraulic fracturing in south-central Oklahoma, *Bull. Seismol. Soc. Am.*, *103*, 1784–1792, doi:10.1785/0120120109.
Hornbach, M. J., et al. (2015), Causal factors for seismicity near Azle, Texas, *Nat. Commun.*, *6*(6728), doi:10.1038/ncomms7728.
Horner, R. B., J. E. Barclay, and J. M. MacRae (1994), Earthquakes and hydrocarbon production in the Fort St. John area of northeastern British Columbia, *Can. J. Explor. Geophys.*, *30*(1), 39–50.
King, G. E. (2010), Thirty years of gas shale fracturing: What have we learned?, paper presented at SPE Annual Technical Conference and Exhibition, Soc. of Petroleum Eng., Florence, Italy, 19–22 Sept., doi:10.2118/133456-MS.
Kummerow, J., Dinske, C., Haring, M., and Asanuma, H. (2014), Induced repeating earthquakes: An indicator for pore pressure changes?, paper presented at Fifth EAGE Passive Seismic Workshop, EAGE, 28 Sept., doi:10.3997/2214-4609.20142161.
Kwiatek, G., P. Martínez-Garzón, G. Dresen, M. Bohnhoff, H. Sone, and C. Hartline (2015), Effects of long-term fluid injection on induced seismicity parameters and maximum magnitude in northwestern part of The Geysers geothermal field, *J. Geophys. Res. Solid Earth*, *120*, 7085–7101, doi:10.1002/2015JB012362.
Laske, G., G. Masters, Z. Ma, and M. Pasyanos (2013), Update on CRUST1.0—A 1-degree global model of Earth's crust, in *EGU General Assembly Conference Abstracts*, vol. 15, p. 2658.
Martínez-Garzón, P., M. Bohnhoff, G. Kwiatek, and G. Dresen (2013), Stress tensor changes related to fluid injection at The Geysers geothermal field, California, *Geophys. Res. Lett.*, *40*, 2596–2601, doi:10.1002/grl.50438.
McGarr, A. (2014), Maximum magnitude earthquakes induced by fluid injection, *J. Geophys. Res. Solid Earth*, *119*, 1008–1019, doi:10.1002/2013JB010597.
Murray, S. (2016), Hydraulic fracturing: Minimizing the risk M.Sc. Thesis, Ludwig-Maximilian Univ. Munich.
Raleigh, C. B., J. H. Healy, and J. D. Bredehoeft (1976), An experiment in earthquake control at Rangley, Colorado, *Science*, *191*, 1230–1237, doi:10.1126/science.191.4233.1230.
Reiter, K., and O. Heidbach (2014), 3-D geomechanical-numerical model of the contemporary crustal stress state in the Alberta Basin (Canada), *Solid Earth*, *5*(2), 1123, doi:10.5194/se-5-1123-2014.
Reiter, K., O. Heidbach, D. Schmitt, K. Haug, M. Ziegler, and I. Moeck (2014), A revised crustal stress orientation database for Canada, *Tectonophysics*, *636*, 111–124, doi:10.1016/j.tecto.2014.08.006.
Reyes, C. G., and M. E. West (2011), The Waveform Suite: A robust platform for manipulating waveforms in MATLAB, *Seismol. Res. Lett.*, *82*, 104–110, doi:10.1785/gssrl.82.1.104.
Rodgers, B. (2014), Declining costs enhance Duvernay shale economics, *Oil Gas J.*, *112*(9), 70–70.
Rokosh, C. D., et al. (2012), Summary of Alberta's shale- and siltstone-hosted hydrocarbon resource potential; Energy Resources Conservation Board, ERCB/AGS Open File Report 2012–06, p. 327.
Schaff, D. P. (2008), Semiempirical statistics of correlation-detector performance, *Bull. Seismol. Soc. Am.*, *98*, 1495–1507, doi:10.1785/0120060263.
Schoenball, M., L. Dorbath, E. Gaucher, J. F. Wellmann, and T. Kohl (2014), Change of stress regime during geothermal reservoir stimulation, *Geophys. Res. Lett.*, *41*, 1163–1170, doi:10.1002/2013GL058514.
Schultz, R., and V. Stern (2015), The Regional Alberta Observatory for Earthquake Studies Network (RAVEN), *CSEG Recorder*, *40*(8), 34–37.
Schultz, R., V. Stern, and Y. J. Gu (2014), An investigation of seismicity clustered near the Cordel Field, west central Alberta, and its relation to a nearby disposal well, *J. Geophys. Res. Solid Earth*, *119*, 3410–3423, doi:10.1002/2013JB010836.
Schultz, R., V. Stern, M. Novakovic, G. Atkinson, and Y. J. Gu (2015a), Hydraulic fracturing and the Crooked Lake Sequences: Insights gleaned from regional seismic networks, *Geophys. Res. Lett.*, *42*, 2750–2758, doi:10.1002/2015GL063455.
Schultz, R., S. Mei, D. Pană, V. Stern, Y. J. Gu, A. Kim, and D. Eaton (2015b), The Cardston Earthquake Swarm and hydraulic fracturing of the Exshaw ("Alberta Bakken" play), *Bull. Seismol. Soc. Am.*, *150*(6), doi:10.1785/0120150131.
Schultz, R., V. Stern, Y. J. Gu, and D. Eaton (2015c), Detection threshold and location resolution of the Alberta Geological Survey earthquake catalogue, *Seismol. Res. Lett.*, *86*(2A), 385–397, doi:10.1785/0220140203.
Schultz, R., H. Corlett, K. Haug, K. Kocon, K. MacCormack, V. Stern, and T. Shipman (2016), Linking fossil reefs with earthquakes: Geologic insight to where induced seismicity occurs in Alberta, *Geophys. Res. Lett.*, *43*, 2534–2542, doi:10.1002/2015GL067514.
Segall, P., and S. Lu (2015), Injection-induced seismicity: Poroelastic and earthquake nucleation effects, *J. Geophys. Res. Solid Earth*, *120*, 5082–5103, doi:10.1002/2015JB012060.
Shapiro, S. A., C. Dinske, and J. Kummerow (2007), Probability of a given-magnitude earthquake induced by a fluid injection, *Geophys. Res. Lett.*, *34*, L22314, doi:10.1029/2007GL031615.
Shapiro, S. A., C. Dinske, C. Langenbruch, and F. Wenzel (2010), Seismogenic index and magnitude probability of earthquakes induced during reservoir fluid stimulations, *Leading Edge*, *29*(3), 304–309, doi:10.1190/1.3353727.

Skoumal, R. J., M. R. Brudzinski, and B. S. Currie (2015a), Earthquakes induced by hydraulic fracturing in Poland Township, Ohio, *Bull. Seismol. Soc. Am.*, *105*, 189–197, doi:10.1785/0120140168.

Skoumal, R. J., M. R. Brudzinski, and B. S. Currie (2015b), Distinguishing induced seismicity from natural seismicity in Ohio: Demonstrating the utility of waveform template matching, *J. Geophys. Res. Solid Earth*, *120*, 6284–6296, doi:10.1002/2015JB012265.

Soltanzadeh, M., G. Davis, A. Fox, D. Hume, and N. Rahim (2015), Application of mechanical and mineralogical rock properties to identify fracture fabrics in the Devonian Duvernay formation in Alberta. Unconventional Resources Technology Conference (URTEC).

Stern, V. H., R. J. Schultz, L. Shen, Y. J. Gu, and D. W. Eaton (2013), Alberta earthquake catalogue, version 1.0, September 2006 through December 2010, *Alberta Geol. Surv. Open–File Rept.*, *15*, 36.

Stoakes, F. A. (1980), Nature and control of shale basin fill and its effect on reef growth and termination: Upper Devonian Duvernay and Ireton Formations of Alberta, Canada, *Bull. Can. Pet. Geol.*, *28*(3), 345–410.

Switzer, S. B., W. G. Holland, D. S. Christie, G. C. Graf, A. S. Hedinger, R. J. McAuley, R. Wierzbicki, and J. J. Packard (1994), Devonian Woodbend-Winterburn strata of the Western Canada Sedimentary Basin, in *Geological Atlas of the Western Canada Sedimentary Basin: Canadian Society of Petroleum Geologists and Alberta Research Council*, edited by G. D. Mossop and I. Shetsen, pp. 165–202, [Available at http://ags.aer.ca/publications/atlas-of-the-western-canada-sedimentary-basin.htm#Publications%20FAQ.]

Vavryčuk, V. (2015), Inversion for the composite moment tensor, *Bull. Seismol. Soc. Am.*, *105*(6), 3024–3035, doi:10.1785/0120150163.

Waldhauser, F., and W. L. Ellsworth (2000), A double difference earthquakes location algorithm: Method and application to the northern Hayward Fault, California, *Bull. Seismol. Soc. Am.*, *90*, 1353–1368, doi:10.1785/0120000006.

Wang, R., Y. J. Gu, R. Schultz, A. Kim, and G. Atkinson (2016), Source analysis of a potential hydraulic fracturing induced earthquake near Fox Creek, Alberta, *Geophys. Res. Lett.*, *43*, 564–573, doi:10.1002/2015GL066917.

Weissenberger, J. A., and K. Potma (2001), The Devonian of western Canada—Aspects of a petroleum system: Introduction, *Bull. Can. Pet. Geol.*, *49*(1), 1–6, doi:10.2113/gscpgbull.49.1.1.

Yenier, E., G. Atkinson, S. Karimi, and D. Baturan (2016), Prediction of earthquake ground motions in western Alberta. Poster Presentation, Seism. Soc. Am., April, 2016, Reno, Nev.

Zhang, H., D. W. Eaton, G. Li, Y. Liu, and R. M. Harrington (2016), Discriminating induced seismicity from natural earthquakes using moment tensors and source spectra, *J. Geophys. Res. Solid Earth*, *121*, 972–993, doi:10.1002/2015JB012603.

Zhang, Y., et al. (2013), Hydrogeologic controls on induced seismicity in crystalline basement rocks due to fluid injection into basal reservoirs, *Groundwater*, *51*(4), 525–538, doi:10.1111/gwat.12071.

Erratum

In the originally published version of this article, text was omitted from the caption of Figure S2 in the Supporting Information S1 file. The file has since been updated and this version may be considered the authoritative version of record.